Supplementary Materials for

Mechanism of allosteric modulation of P-glycoprotein by transport substrates and inhibitors

Reza Dastvan, Smriti Mishra, Yelena B. Peskova, Robert K. Nakamoto, Hassane S. Mchaourab*

*Corresponding author. Email: hassane.mchaourab@vanderbilt.edu

Published 17 May 2019, *Science* **364**, 689 (2019)
DOI: 10.1126/science.aav9406

This PDF file includes:

Materials and Methods

No statistical methods were used to predetermine sample size. The experiments were not randomized. The investigators were not blinded to allocation during experiments and outcome assessment.

Cloning and expression

On a cysteine-less (CL) background, double-cysteine mutant constructs of the mouse orthologue of ABCB1 (Abcb1a, also known as P-glycoprotein or *Mdr3*) were utilized and expressed in Sf21 cells as previously described (*8*). Validity of mutations was confirmed by sequencing.

Purification and spin labeling

Membrane isolation, purification and spin labeling were performed as described previously (*8*). The spin-labelled Pgp was then separated from excess spin label and free micelles by size-exclusion chromatography in Gel Filtration Buffer (50 mM Tris-HCl, 50 mM NaCl, 20% glycerol (v/v), 0.05% β-DDM, pH 7.4 at 4 °C). Purity of Pgp was assessed by SDS–PAGE.

Reconstitution in nanodiscs

The lipids (3:2 w/w *E. coli* polar lipids:L-α-phosphatidylcholine) were dissolved in chloroform, evaporated to dryness on a rotary evaporator, and desiccated overnight under vacuum. The lipids were hydrated in Gel Filtration Buffer (50 mM Tris-HCl, 50 mM NaCl, pH 7.4 at 4 °C) to yield a final lipid concentration of 20 mM. Lipids were vortexed and subjected to 10 freeze-thaw cycles in liquid nitrogen/warm water and stored in small aliquots at −80 °C. Membrane scaffold protein (MSP1D1E3) was expressed and purified as described previously (*11*). For reconstitution into nanodiscs, purified spin-labeled proteins in 0.05% β-DDM micelles were mixed with lipids, MSP1D1E3 and sodium cholate in the following molar ratios: MSP1D1E3:protein, 10:1; lipid:MSP1D1E3, 110:1; β-DDM+cholate:lipid, 5:1. Mixtures were rocked at 4°C for one hour. The detergent was removed using four cycles of stepwise Bio-Beads (Bio-Rad) addition (in total 0.6 g/ml), in the following sequence: first and second additions (0.1 g/ml, one-hour incubation), third addition (0.2 g/ml, overnight), and fourth addition (0.2 g/ml, one-hour incubation). The reconstitution solution was filtered using 0.45 μm filter to remove the Bio-Beads. Nanodiscs containing Pgp were separated from empty nanodiscs by size-exclusion chromatography using a Superdex 200 Increase column (GE Healthcare) in the Gel Filtration buffer with 10% glycerol (v/v). Gel filtration fractions with reconstituted Pgp were identified by SDS-PAGE. Nanodiscs were concentrated using an Amicon Ultra-100 kDa centrifugal filter. Concentration of spin labeled mutants in nanodiscs was determined as described previously (*31*) by comparing the intensity of the integrated continuous wave electron paramagnetic resonance (CW EPR) spectrum to that of the same mutant in detergent micelles. Concentration of the nanodisc-reconstituted CL Pgp was determined by SDS-PAGE using a standard curve.

DEER sample preparation

For the mixed lipid/detergent micelle sample preparation, Pgp was concentrated to about 70-90 mM using Amicon Ultra-100 kDa centrifugal filters (Millipore). Pgp sample preparation was as described previously with 7 min incubation at 37 °C for DEER spectroscopy (*8*). For mixed micelle samples, the molar ratio of protein:lipid:detergent is 1:105:12.7. The lipids were suspended in Tris buffer (pH 6.9) as a mixture (3:2 w/w *Escherichia coli* polar lipids:L-α-phosphatidylcholine) from Avanti Polar Lipids, to a final concentration of 50 mg ml^{-1}. Protein, extra β-DDM in gel filtration buffer and lipids were mixed until homogeneous. Nucleotides and substrates were then subsequently mixed and incubated. The final concentrations of ATP, vanadate, and $MgSO_4$, were 10 mM, 2 mM, and 10 mM, respectively. Stock solutions of substrates and inhibitors were prepared in dimethyl sulfoxide (final concentration of DMSO was kept less than 2%). For the mixed micelle sample preparation, the concentration of substrates and inhibitors (tariquidar and zosuquidar) were 0.4 mM, and 0.2 mM, respectively. For the NBS2 pair 511-1043 in mixed micelles, utilized concentrations are shown in Table S1. For the nanodiscs sample preparation, the concentration of substrates and inhibitors were 0.4 mM, and 0.1 mM, respectively. For the NBS2 pairs, 511-1043 and 511-1043-E552Q-E1197Q, concentrations are shown in Table S2. Nanodiscs samples were first incubated with substrates or inhibitors at 37 °C for 3 min prior to the addition of other components.

ATPase assay

The specific ATPase activity of Pgp was determined by an inorganic phosphate assay as previously described (*32*) with the following modifications. For ATPase assays in mixed micelles, 6 μg of Pgp with an equal amount (w/w) of *E. coli* polar lipids:L-α-phosphatidylcholine (3:2 w/w) were incubated for 10 min at 37 °C in the basal (no substrate) or substrate-stimulated conditions with increasing concentrations of ATP (performed in duplicate). The reaction was stopped by adding 1 volume of 12% SDS and color was developed using a 1:1 solution of ammonium molybdate (2% in 1 M HCl) and ascorbic acid (12% in 1 M HCl). The absorbance at 850 nm was measured on a BioTek Synergy H4 microplate reader. The amount of hydrolyzed phosphate was determined by comparison to an inorganic phosphate standard curve. For ATPase assays in nanodiscs, 3 μg of Pgp was first incubated with substrates or inhibitors at 37 °C for 3 min prior to the addition of ATP.

DEER spectroscopy and data analysis

DEER spectroscopy was performed on an Elexsys E580 EPR spectrometer operating at Q-band frequency (33.9 GHz) equipped with a 10W Amp-Q amplifeier (Bruker) with the dead-time free four-pulse sequence at 83 K (*8, 33*). The pulse lengths were 10 ns ($\pi/2$) and 20 ns (π) for the probe pulses and 40 ns for the pump pulse. The frequency separation was 63 MHz. Primary DEER decays were analyzed using home-written software operating in the Matlab environment (*34, 35*). Briefly, the software carries out global analysis of the DEER decays obtained under different conditions for the same spin-labeled position. The distance distribution is assumed to consist of a sum of Gaussians, the number and population of which are determined based on a statistical criterion. Distance distributions on the structures were predicted *in silico* using a rotamer library approach by MMM 2013.2 software package (*36*). Rotamer calculations were conducted using the 298 K rotamer library.

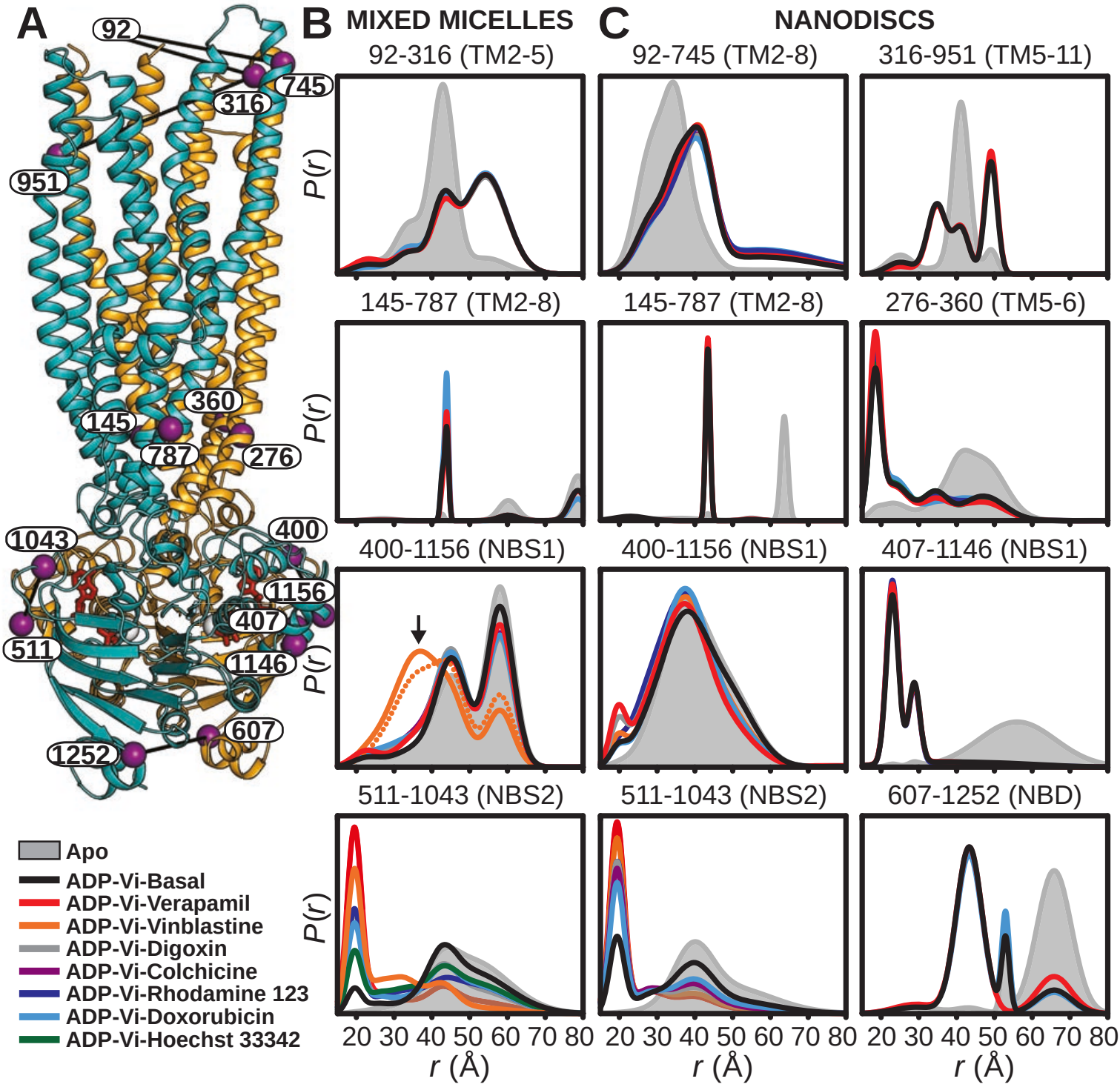

Fig. S1. Distance distributions in the high energy post ATP-hydrolysis state (HES). (**A**) Ribbon representation of the OF Pgp highlighting the positions of spin label pairs as purple spheres with the N- and C-terminal halves colored with orange and cyan respectively. Distance distributions in (**B**) mixed micelles and (**C**) lipid nanodiscs are shown for the apo state, basal (ADP-Vi-Basal) and substrate-coupled HES in the presence of different substrates. In mixed micelles, vinblastine (orange) at the inhibitory concentrations of 0.4 (solid line) and 0.2 mM (dotted line) exhibits a distinct shorter distance (arrow) at the NBS1 A-loop pair 400-1156. In addition, the NBS2 A-loop pair 511-1043 exhibits distinct HES signatures for different substrates.

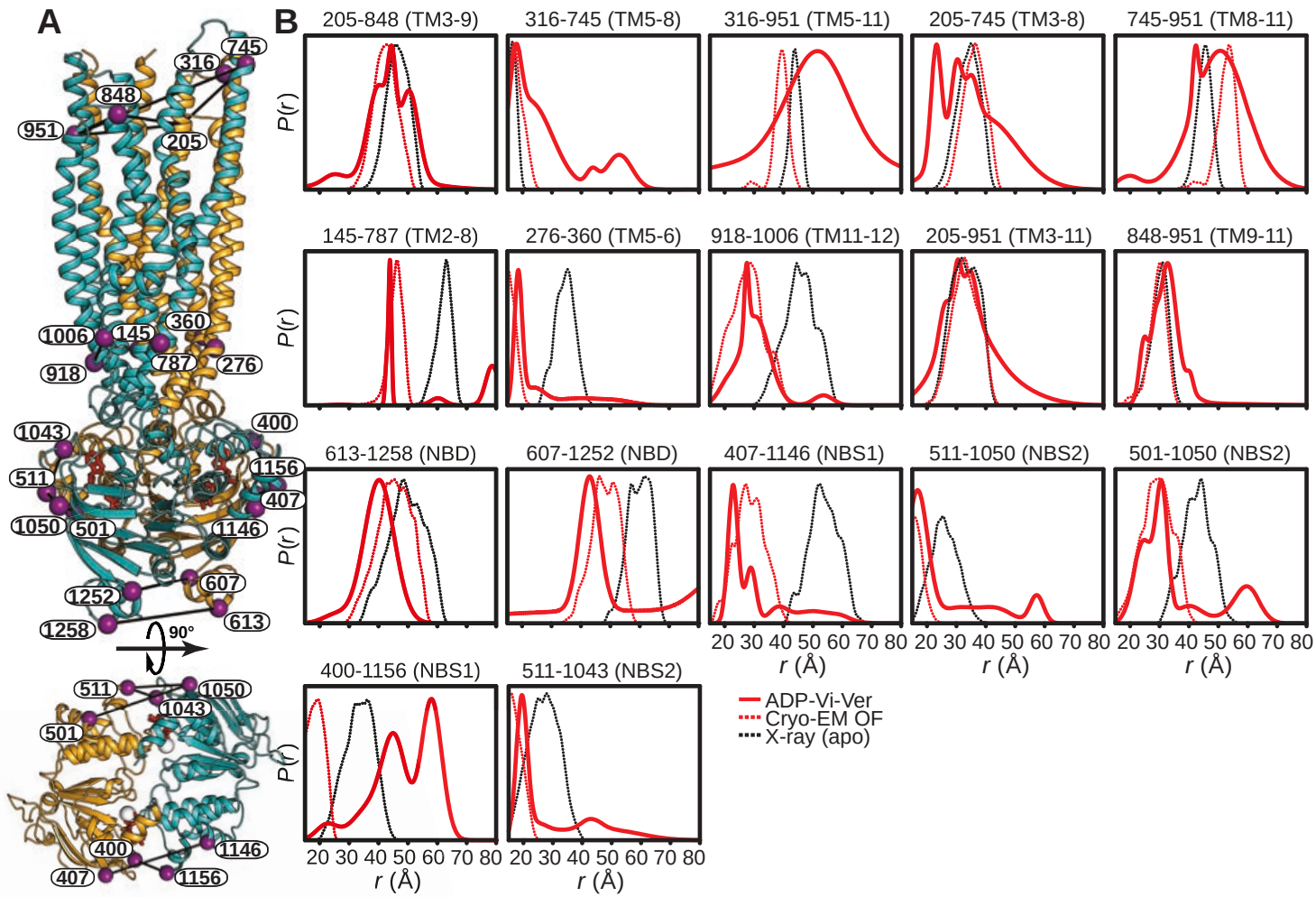

Fig. S2. Comparison of distance distributions in the HES to predicted distributions calculated from the cryo-EM OF structure. (**A**) Ribbon representation of the OF Pgp highlighting the location of spin label pairs as purple spheres. (**B**) Distance distributions in mixed micelles for the HES of ATP hydrolysis in the presence of substrate verapamil (ADP-Vi-Ver) (solid lines) compared with the distributions predicted by the OF and apo (PDB codes 6C0V and 4M1M, respectively) structures (dashed lines). Note the overlap between OF and Apo distance distributions on the extracellular side. The comparison reveals deviations on the extracellular side and the A-loops of the NBDs as elaborated in the main text. Specifically, the distance distributions at pairs monitoring the A-loops (400-1156 and 511-1043) are predicted by the cryo-EM structure to be symmetric and characterized by dominant short distance components. In the basal cycle, the two pairs have apo-like components, whereas in the presence of substrates, they are asymmetric with apo-like NBS1 pair and NBS2 displaying a short distance component.

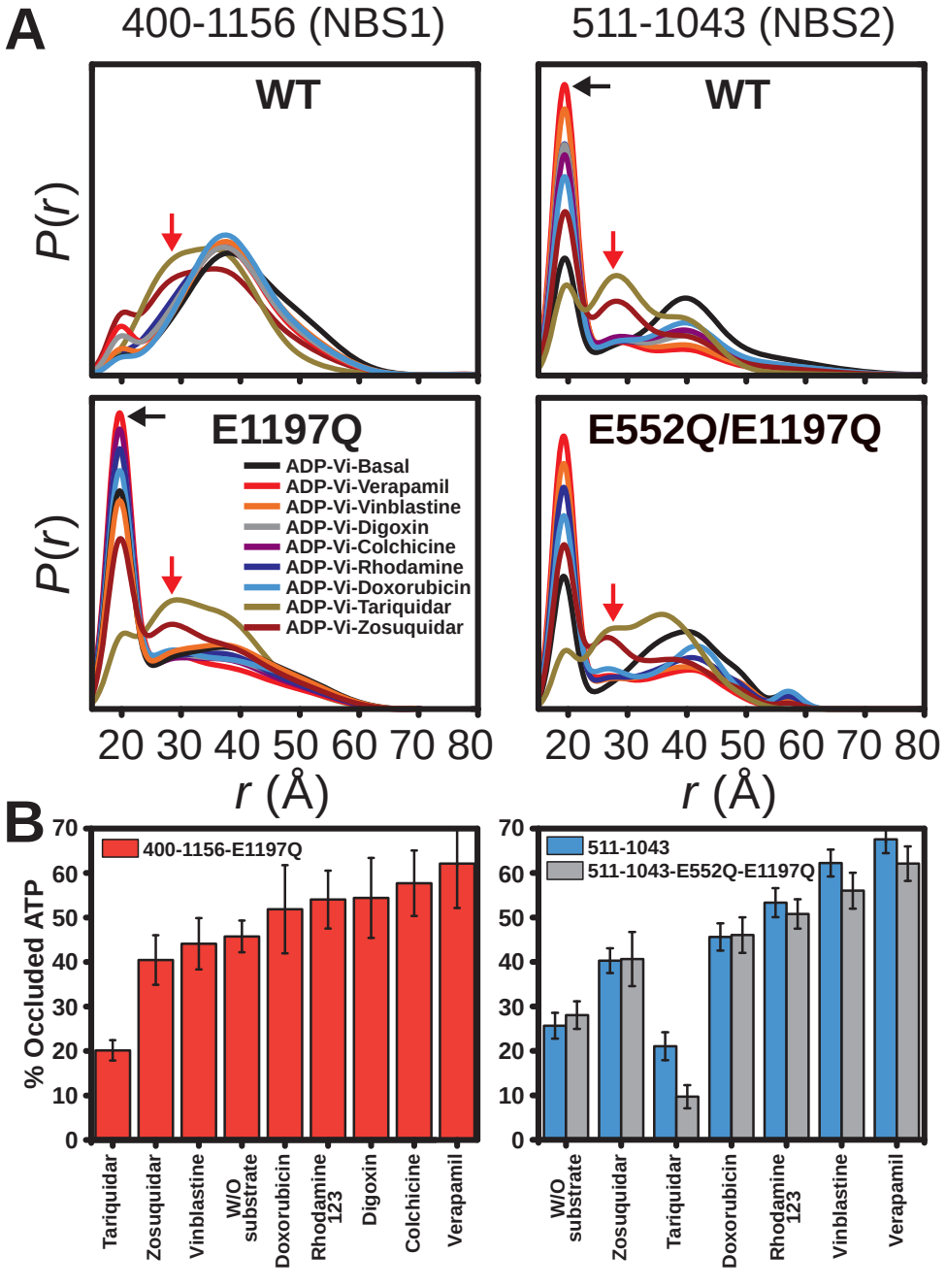

Fig. S3. Catalytic glutamate substitution symmetrize the structure of the NBSs as predicted by the cryoEM structure of the mutant. (**A**) Distance distributions in nanodiscs for NBS1 (400-1156) and NBS2 (511-1043) A-loop pairs in the WT and Walker B mutations backgrounds. The E1197Q substitution reverses the asymmetry between the two NBSs as manifested by the short distance component in NBS1 and its absence at NBS2 (data not shown and reference *8*). However neither the single nor the double E-to-Q substitution abolish the dependence of the short component on substrates and inhibitors. Furthermore, the inhibitory effect of vinblastine at NBS1 can be detected in this background. Inhibitors induce a distinct conformation at the A-loop regions (indicated by red arrows). (**B**) Population of the occluded ATP conformation is plotted as a function of substrates and inhibitors.

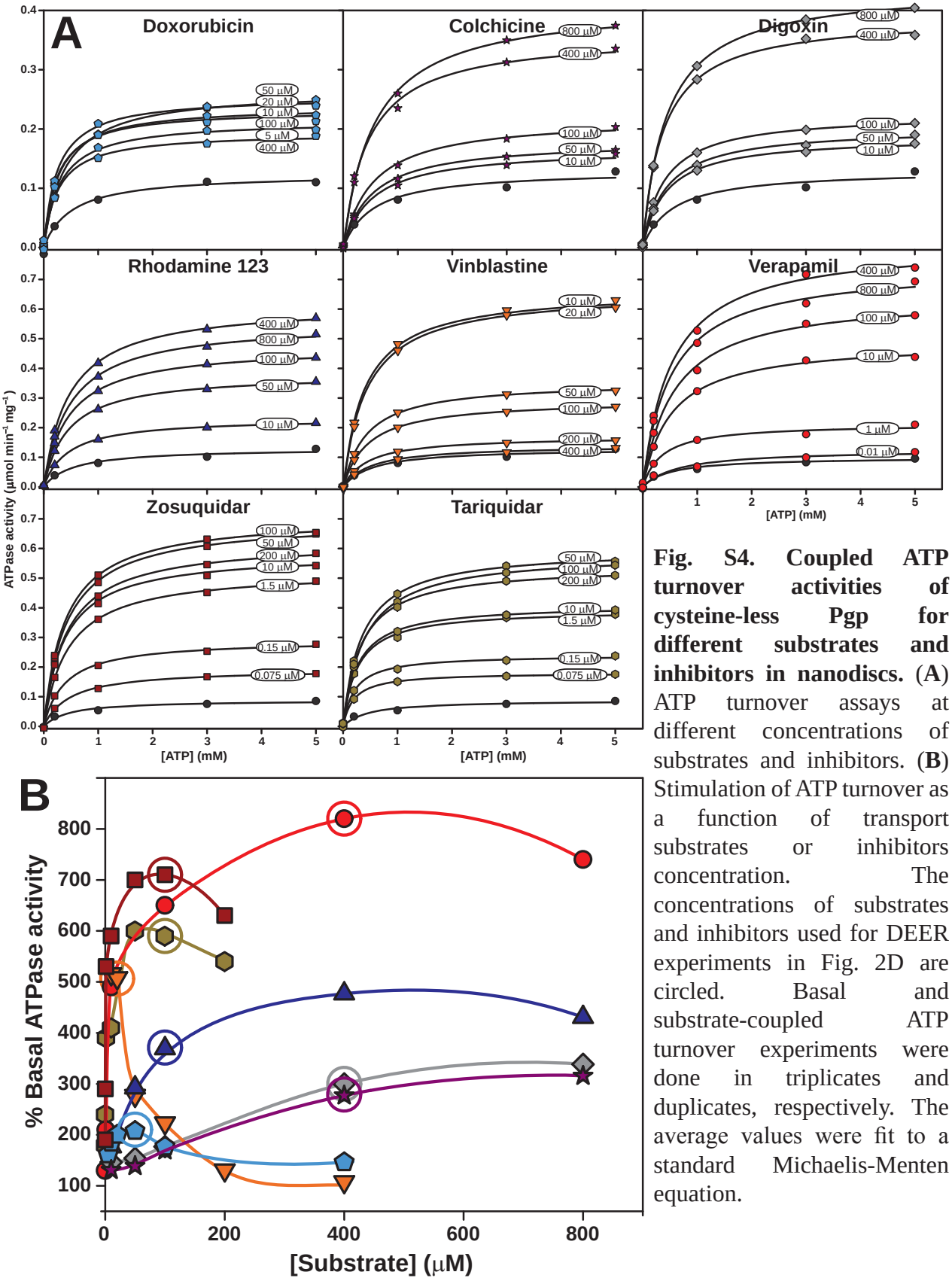

Fig. S4. Coupled ATP turnover activities of cysteine-less Pgp for different substrates and inhibitors in nanodiscs. (**A**) ATP turnover assays at different concentrations of substrates and inhibitors. (**B**) Stimulation of ATP turnover as a function of transport substrates or inhibitors concentration. The concentrations of substrates and inhibitors used for DEER experiments in Fig. 2D are circled. Basal and substrate-coupled ATP turnover experiments were done in triplicates and duplicates, respectively. The average values were fit to a standard Michaelis-Menten equation.

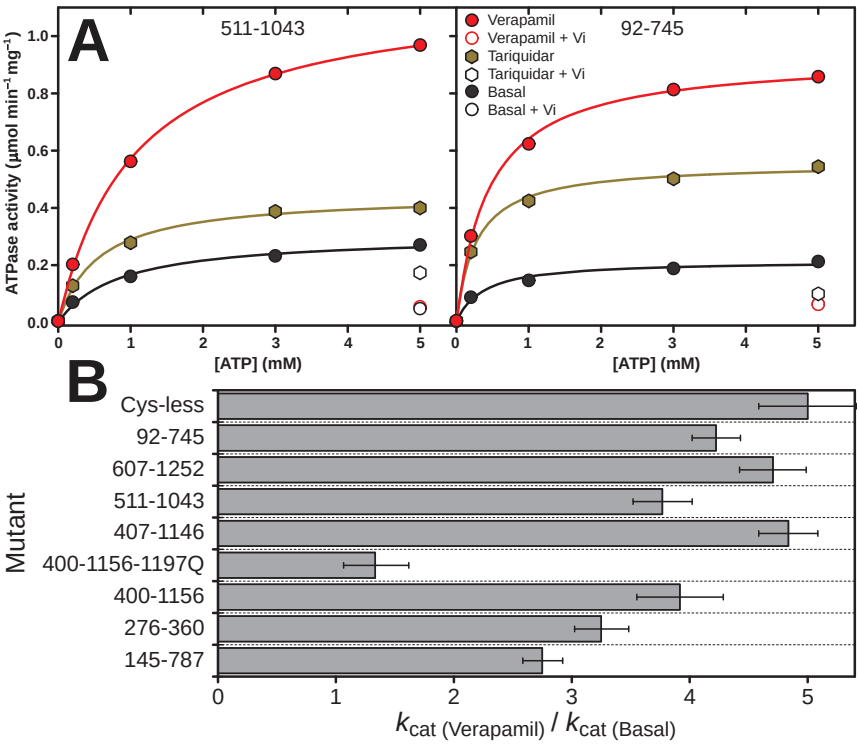

Fig. S5. Coupled ATP turnover activities of Pgp mutants in nanodiscs. (**A**) Representative ATPase assays on Pgp mutants in nanodiscs. Basal (black) and verapamil- (red) and tariquidar-stimulated (dark yellow) ATP hydrolysis were measured by Pi-release. The single data points represent the release rate under vanadate trapping condition (5 mM ATP, 2 mM vanadate). (**B**) The stimulation of ATPase activity for mutants with intact NBSs and with catalytic glutamate substitutions in nanodiscs compared to cysteine-less Pgp. Basal and substrate-coupled ATP turnover experiments were done in triplicates and duplicates, respectively. The average values were fit to a standard Michaelis-Menten equation.

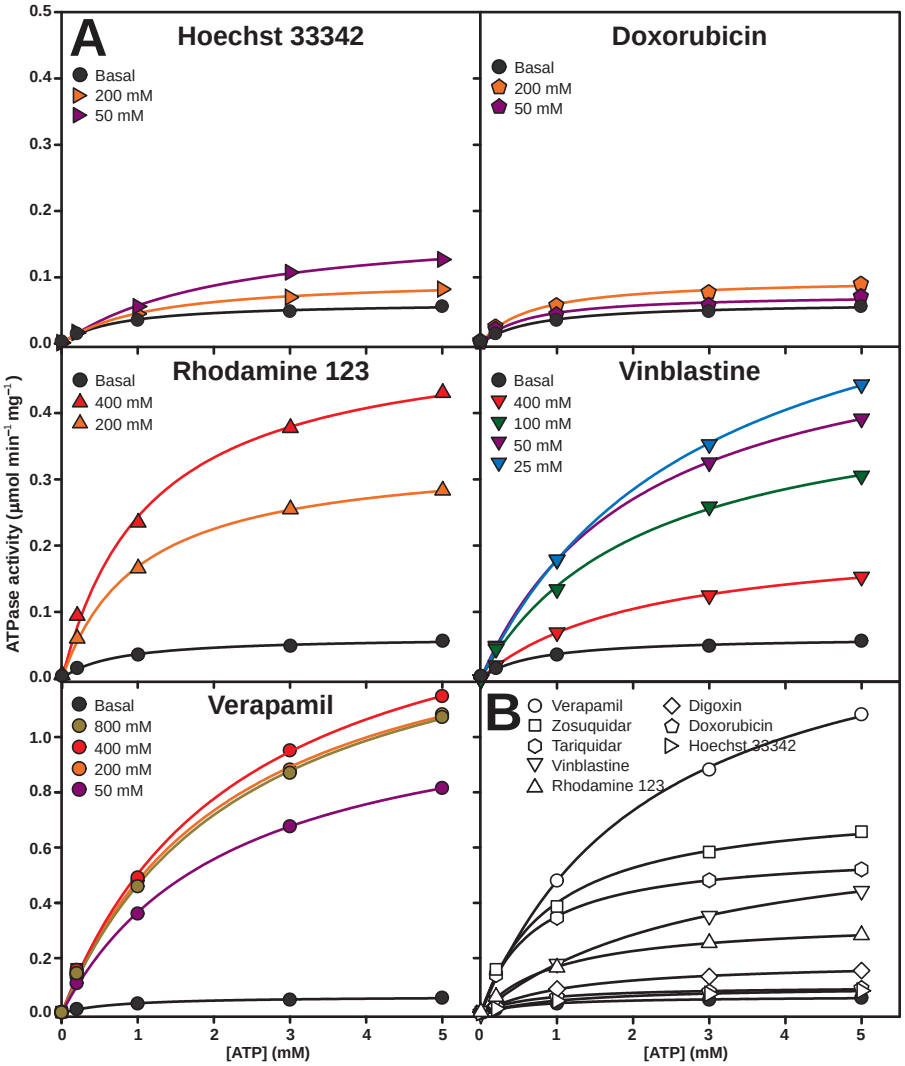

Fig. S6. Coupled ATP turnover activities of cysteine-less Pgp for different substrates and inhibitors in mixed micelles. (**A**) ATP turnover assays at different concentrations of substrates. (**B**) Basal and stimulated ATP turnover activities of the cysteine-less Pgp for different substrates and inhibitors under the concentrations utilized for DEER experiments in fig. S7D. Basal and substrate-coupled ATP turnover experiments were done in triplicates and duplicates, respectively. The average values were fit to a standard Michaelis-Menten equation.

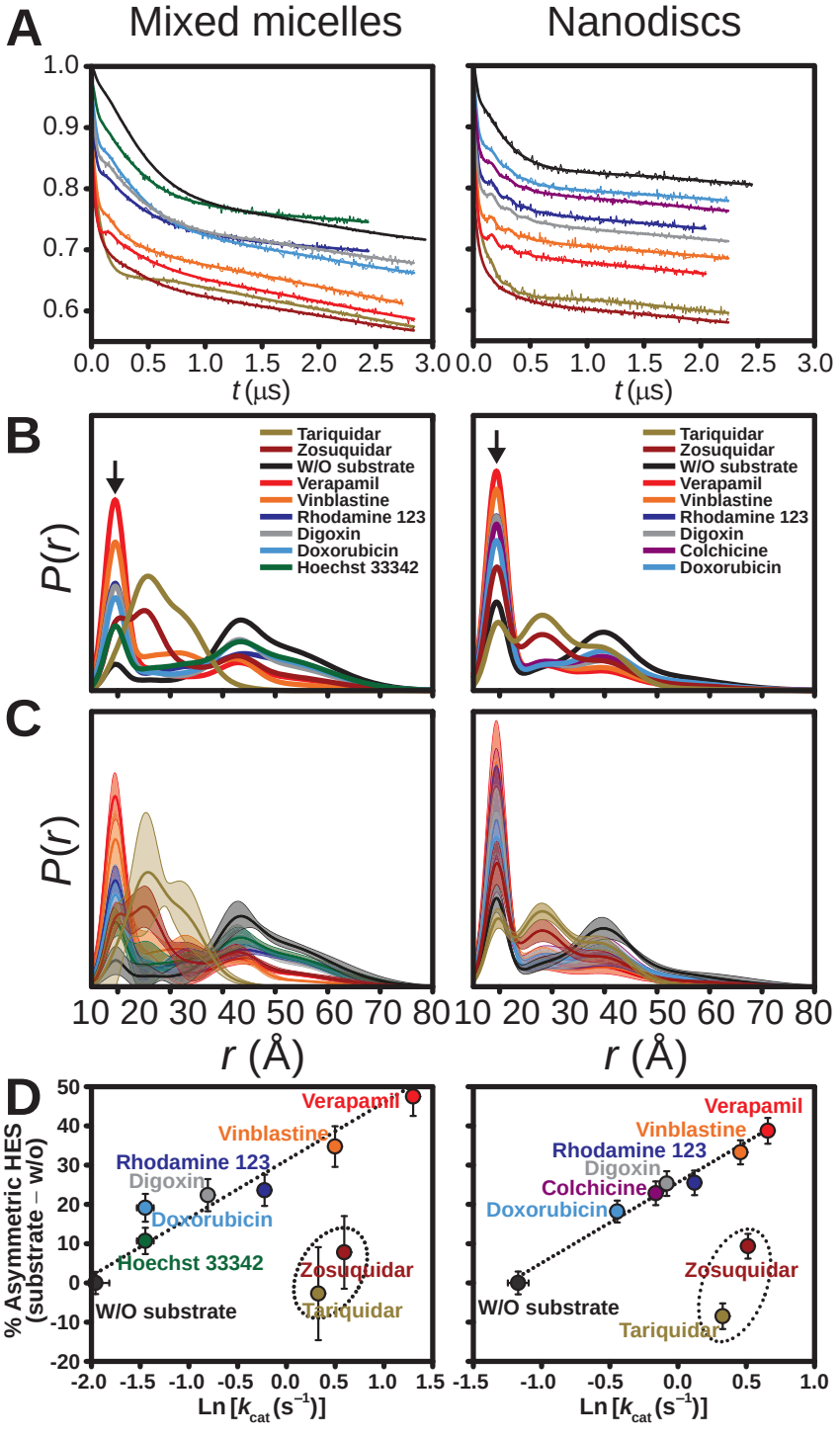

Fig. S7. DEER data analysis for the NBS2 A-loop pair 511-1043. (**A**) Primary DEER traces along with the fits for the ADP-Vi condition in the presence and absence of substrates and inhibitors, (**B**) the obtained distance distributions from global analysis of the DEER decays under different conditions, and (**C**) error analysis of distributions for each condition. Confidence bands (2σ) for distance distributions are shown about the best fit line for each substrate. These bands, which depict the estimated uncertainty in $P(r)$, reflect error associated with the noise and background factor in the fitting of the primary DEER traces (*34*). For each experimental condition, Gaussian components are described by a distance r, the width and the fractional population. The error bars in panel D, Fig. 2D and fig. S3B for the population of the occluded ATP conformation calculated from the short distance component, represent the uncertainty in this fit parameter reported at the 2σ (95%) confidence level. (**D**) Comparison of the dependence of the asymmetric HES population on the k_{cat} for different substrates and inhibitors in mixed micelles and nanodiscs.

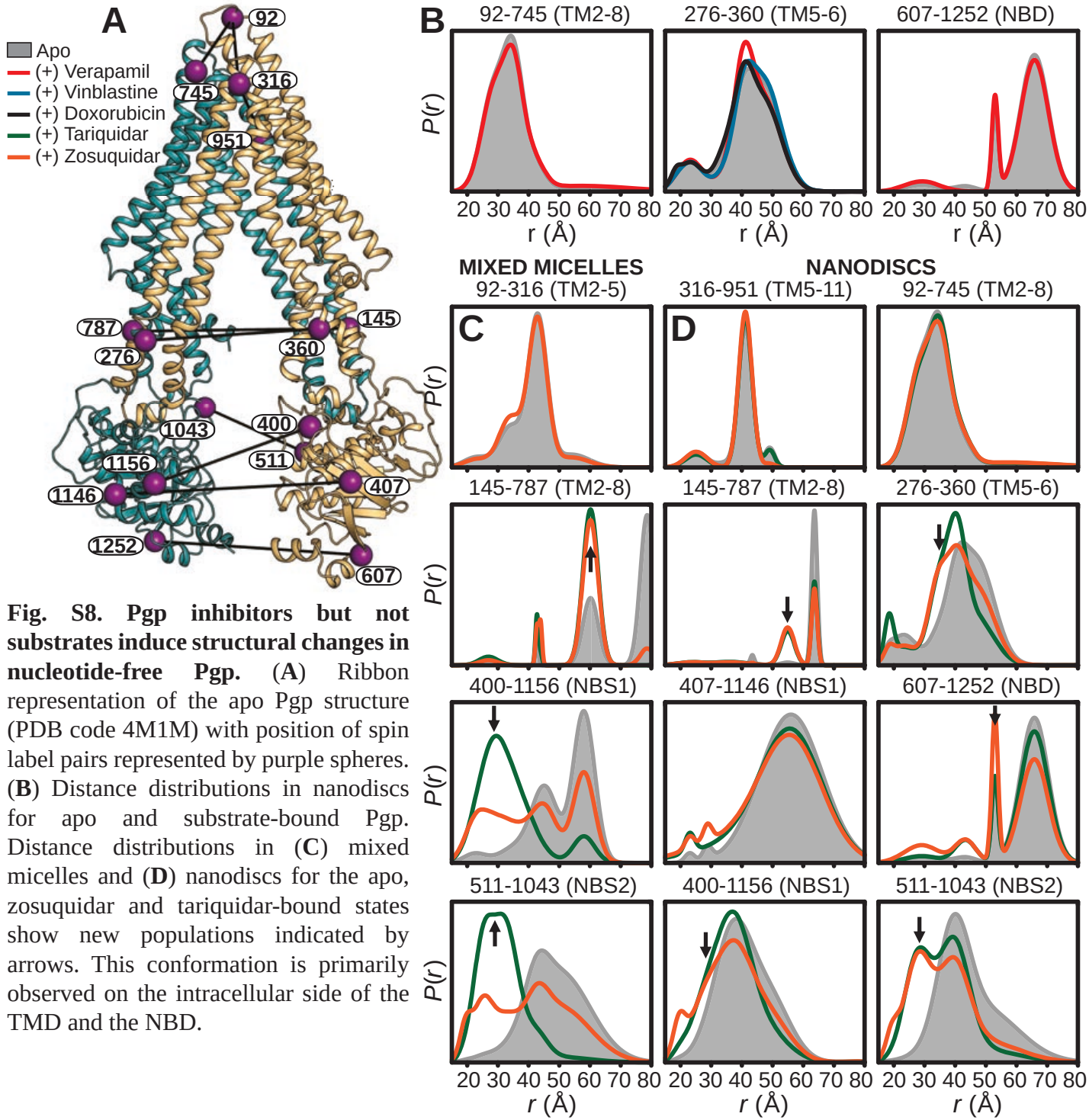

Fig. S8. Pgp inhibitors but not substrates induce structural changes in nucleotide-free Pgp. (**A**) Ribbon representation of the apo Pgp structure (PDB code 4M1M) with position of spin label pairs represented by purple spheres. (**B**) Distance distributions in nanodiscs for apo and substrate-bound Pgp. Distance distributions in (**C**) mixed micelles and (**D**) nanodiscs for the apo, zosuquidar and tariquidar-bound states show new populations indicated by arrows. This conformation is primarily observed on the intracellular side of the TMD and the NBD.

Table S1. Kinetic parameters for ATPase assays on Cys-less Pgp in mixed micelles.

Substrate/inhibitor	k_{cat} [s^{-1}]	$K_{M\ (ATP)}$ [M]
Basal ¶	0.14 ± 0.02 *	$0.72\times10^{-3} \pm 0.16\times10^{-3}$ *
Hoechst 33342 (50 μM)	0.42 ± 0.02	$2.20\times10^{-3} \pm 0.16\times10^{-3}$
Hoechst 33342 (200 μM) ¶	0.24 ± 0.02	$1.17\times10^{-3} \pm 0.15\times10^{-3}$
Doxorubicin (50 μM)	0.19 ± 0.02	$0.62\times10^{-3} \pm 0.18\times10^{-3}$
Doxorubicin (200 μM) ¶	0.24 ± 0.02	$0.65\times10^{-3} \pm 0.14\times10^{-3}$
Digoxin (400 μM) ¶	0.45 ± 0.02	$1.19\times10^{-3} \pm 0.14\times10^{-3}$
Rhodamine 123 (200 μM) ¶	0.80 ± 0.02	$1.02\times10^{-3} \pm 0.07\times10^{-3}$
Rhodamine 123 (400 μM)	1.25 ± 0.05	$1.15\times10^{-3} \pm 0.15\times10^{-3}$
Vinblastine (25 μM) ¶	1.65 ± 0.05	$2.91\times10^{-3} \pm 0.10\times10^{-3}$
Vinblastine (50 μM)	1.32 ± 0.02	$2.12\times10^{-3} \pm 0.04\times10^{-3}$
Vinblastine (100 μM)	1.03 ± 0.05	$2.15\times10^{-3} \pm 0.22\times10^{-3}$
Vinblastine (400 μM)	0.52 ± 0.02	$2.17\times10^{-3} \pm 0.13\times10^{-3}$
Tariquidar (200 μM) ¶	1.39 ± 0.02	$0.68\times10^{-3} \pm 0.03\times10^{-3}$
Zosuquidar (200 μM) ¶	1.81 ± 0.07	$0.92\times10^{-3} \pm 0.11\times10^{-3}$
Verapamil (50 μM)	2.77 ± 0.07	$2.21\times10^{-3} \pm 0.12\times10^{-3}$
Verapamil (200 μM) ¶	3.67 ± 0.09	$2.25\times10^{-3} \pm 0.13\times10^{-3}$
Verapamil (400 μM)	3.97 ± 0.14	$2.35\times10^{-3} \pm 0.20\times10^{-3}$
Verapamil (800 μM)	3.71 ± 0.14	$2.39\times10^{-3} \pm 0.19\times10^{-3}$

* Fit errors

¶ Corresponding ATPase assays and Ln (k_{cat}) values are shown in figs. S6B and S7D, respectively.

Table S2. Kinetic parameters for ATPase assays on Cys-less Pgp in nanodiscs.

Substrate/inhibitor	k_{cat} [s^{-1}]	$K_{M\ (ATP)}$ [M]
Basal ¶	0.31 ± 0.02 *	$0.51\times10^{-3} \pm 0.13\times10^{-3}$ *
Doxorubicin (5 μM)	0.49 ± 0.02	$0.30\times10^{-3} \pm 0.03\times10^{-3}$
Doxorubicin (10 μM)	0.56 ± 0.01	$0.26\times10^{-3} \pm 0.02\times10^{-3}$
Doxorubicin (20 μM)	0.61 ± 0.02	$0.25\times10^{-3} \pm 0.04\times10^{-3}$
Doxorubicin (50 μM) ¶	0.64 ± 0.01	$0.39\times10^{-3} \pm 0.02\times10^{-3}$
Doxorubicin (100 μM)	0.54 ± 0.02	$0.24\times10^{-3} \pm 0.02\times10^{-3}$
Doxorubicin (400 μM)	0.45 ± 0.01	$0.26\times10^{-3} \pm 0.02\times10^{-3}$
Colchicine (10 μM)	0.40 ± 0.02	$0.54\times10^{-3} \pm 0.10\times10^{-3}$
Colchicine (50 μM)	0.42 ± 0.01	$0.52\times10^{-3} \pm 0.03\times10^{-3}$
Colchicine (100 μM)	0.52 ± 0.01	$0.54\times10^{-3} \pm 0.04\times10^{-3}$
Colchicine (400 μM) ¶	0.85 ± 0.02	$0.45\times10^{-3} \pm 0.06\times10^{-3}$
Colchicine (800 μM)	0.96 ± 0.01	$0.56\times10^{-3} \pm 0.02\times10^{-3}$
Digoxin (10 μM)	0.45 ± 0.02	$0.42\times10^{-3} \pm 0.04\times10^{-3}$
Digoxin (50 μM)	0.47 ± 0.02	$0.44\times10^{-3} \pm 0.04\times10^{-3}$
Digoxin (100 μM)	0.54 ± 0.02	$0.40\times10^{-3} \pm 0.03\times10^{-3}$
Digoxin (400 μM) ¶	0.92 ± 0.02	$0.37\times10^{-3} \pm 0.03\times10^{-3}$
Digoxin (800 μM)	1.03 ± 0.02	$0.44\times10^{-3} \pm 0.01\times10^{-3}$
Rhodamine 123 (10 μM)	0.54 ± 0.02	$0.44\times10^{-3} \pm 0.03\times10^{-3}$
Rhodamine 123 (50 μM)	0.89 ± 0.02	$0.45\times10^{-3} \pm 0.02\times10^{-3}$
Rhodamine 123 (100 μM) ¶	1.13 ± 0.01	$0.45\times10^{-3} \pm 0.01\times10^{-3}$
Rhodamine 123 (400 μM)	1.46 ± 0.02	$0.46\times10^{-3} \pm 0.02\times10^{-3}$
Rhodamine 123 (800 μM)	1.32 ± 0.02	$0.48\times10^{-3} \pm 0.03\times10^{-3}$
Vinblastine (10 μM)	1.58 ± 0.02	$0.39\times10^{-3} \pm 0.03\times10^{-3}$
Vinblastine (20 μM) ¶	1.55 ± 0.02	$0.43\times10^{-3} \pm 0.02\times10^{-3}$
Vinblastine (50 μM)	0.85 ± 0.01	$0.43\times10^{-3} \pm 0.02\times10^{-3}$
Vinblastine (100 μM)	0.68 ± 0.01	$0.46\times10^{-3} \pm 0.01\times10^{-3}$
Vinblastine (200 μM)	0.40 ± 0.02	$0.44\times10^{-3} \pm 0.03\times10^{-3}$
Vinblastine (400 μM)	0.33 ± 0.02	$0.50\times10^{-3} \pm 0.06\times10^{-3}$
Verapamil (0.01 μM)	0.31 ± 0.02	$0.66\times10^{-3} \pm 0.23\times10^{-3}$
Verapamil (1 μM)	0.49 ± 0.02	$0.36\times10^{-3} \pm 0.08\times10^{-3}$
Verapamil (10 μM)	1.15 ± 0.02	$0.52\times10^{-3} \pm 0.03\times10^{-3}$
Verapamil (100 μM)	1.53 ± 0.05	$0.57\times10^{-3} \pm 0.06\times10^{-3}$
Verapamil (400 μM) ¶	1.93 ± 0.05	$0.52\times10^{-3} \pm 0.04\times10^{-3}$
Verapamil (800 μM)	1.74 ± 0.05	$0.51\times10^{-3} \pm 0.06\times10^{-3}$
Tariquidar (0.075 μM)	0.42 ± 0.01	$0.20\times10^{-3} \pm 0.03\times10^{-3}$
Tariquidar (0.15 μM)	0.56 ± 0.02	$0.21\times10^{-3} \pm 0.03\times10^{-3}$
Tariquidar (1.5 μM)	0.92 ± 0.02	$0.26\times10^{-3} \pm 0.03\times10^{-3}$
Tariquidar (10 μM)	0.96 ± 0.01	$0.27\times10^{-3} \pm 0.01\times10^{-3}$
Tariquidar (50 μM)	1.41 ± 0.02	$0.34\times10^{-3} \pm 0.02\times10^{-3}$
Tariquidar (100 μM) ¶	1.39 ± 0.02	$0.39\times10^{-3} \pm 0.02\times10^{-3}$
Tariquidar (200 μM)	1.27 ± 0.02	$0.33\times10^{-3} \pm 0.02\times10^{-3}$
Zosuquidar (0.075 μM)	0.45 ± 0.05	$0.48\times10^{-3} \pm 0.19\times10^{-3}$
Zosuquidar (0.15 μM)	0.68 ± 0.05	$0.39\times10^{-3} \pm 0.12\times10^{-3}$
Zosuquidar (1.5 μM)	1.25 ± 0.05	$0.45\times10^{-3} \pm 0.07\times10^{-3}$
Zosuquidar (10 μM)	1.39 ± 0.02	$0.38\times10^{-3} \pm 0.02\times10^{-3}$
Zosuquidar (50 μM)	1.65 ± 0.02	$0.42\times10^{-3} \pm 0.02\times10^{-3}$
Zosuquidar (100 μM) ¶	1.67 ± 0.05	$0.39\times10^{-3} \pm 0.04\times10^{-3}$
Zosuquidar (200 μM)	1.48 ± 0.05	$0.41\times10^{-3} \pm 0.06\times10^{-3}$

* Fit errors

¶ Corresponding Ln (k_{cat}) values are shown in Fig. 2D and fig. S7D.

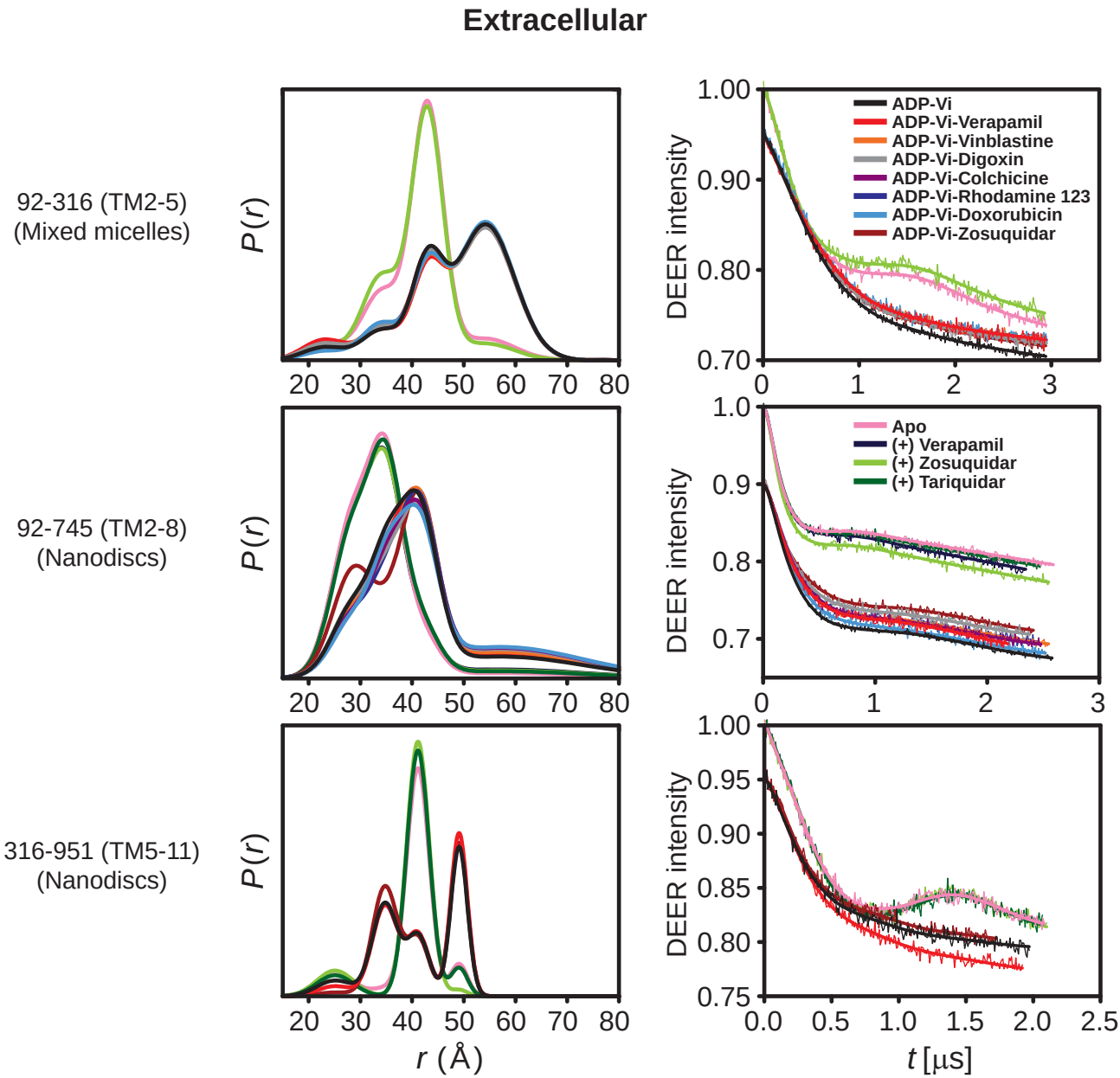

Data Appendix 1. DEER data analysis for the extracellular side of the TMD. For each mutant, from left to right, distance distributions, and the primary DEER traces along with the fits are shown. Normalized DEER traces are shown with y-axis offsets for clarity. In addition, 500 ns at the end of DEER traces are removed (not shown) to reduce the contribution of the artefacts at the end of the trace which could disturb data analysis.

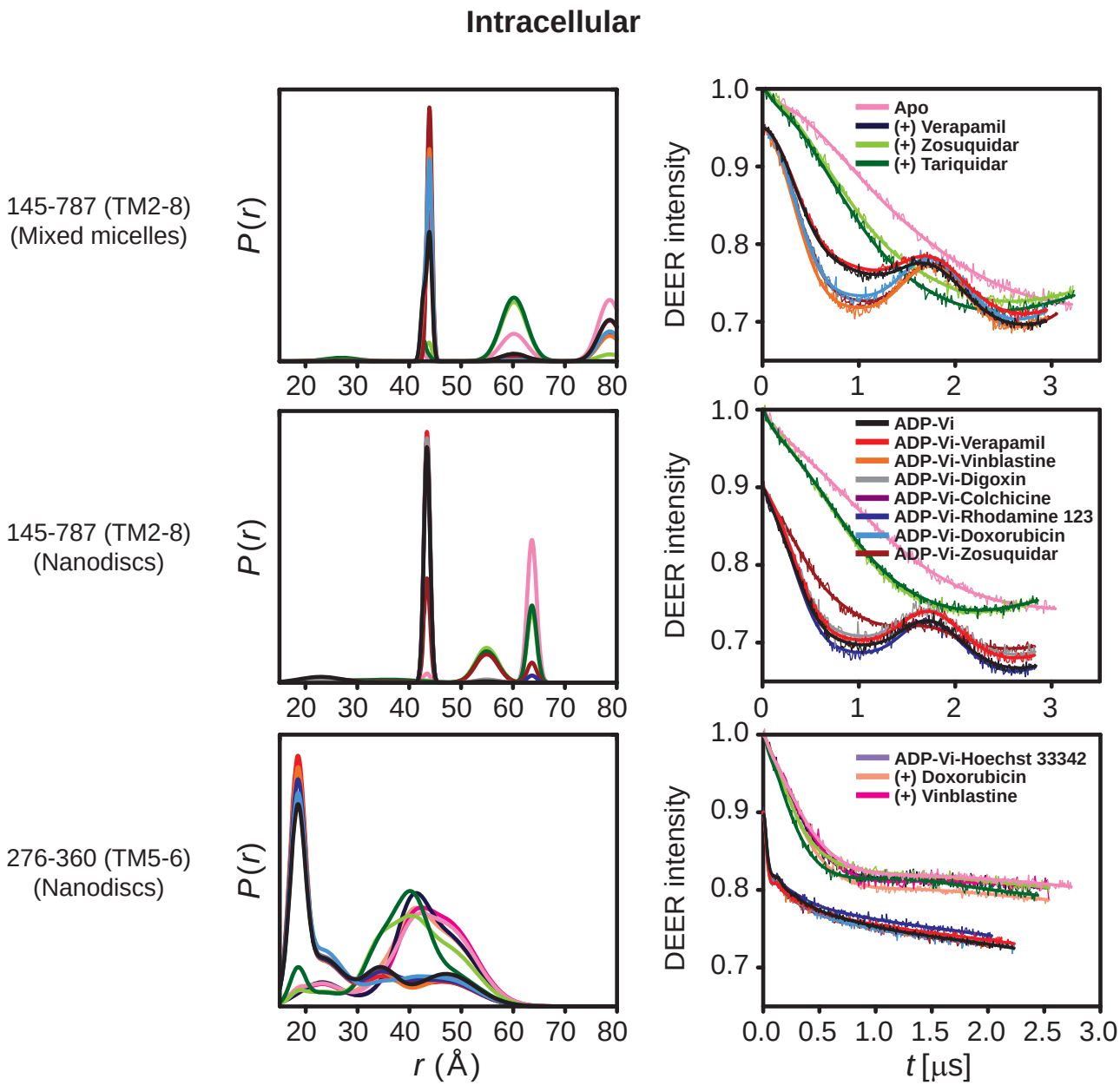

Data Appendix 2. DEER data analysis for the intracellular side of the TMD. For each mutant, from left to right, distance distributions, and the primary DEER traces along with the fits are shown. Normalized DEER traces are shown with y-axis offsets for clarity. In addition, 500 ns at the end of DEER traces are removed (not shown) to reduce the contribution of the artefacts at the end of the trace which could disturb data analysis.

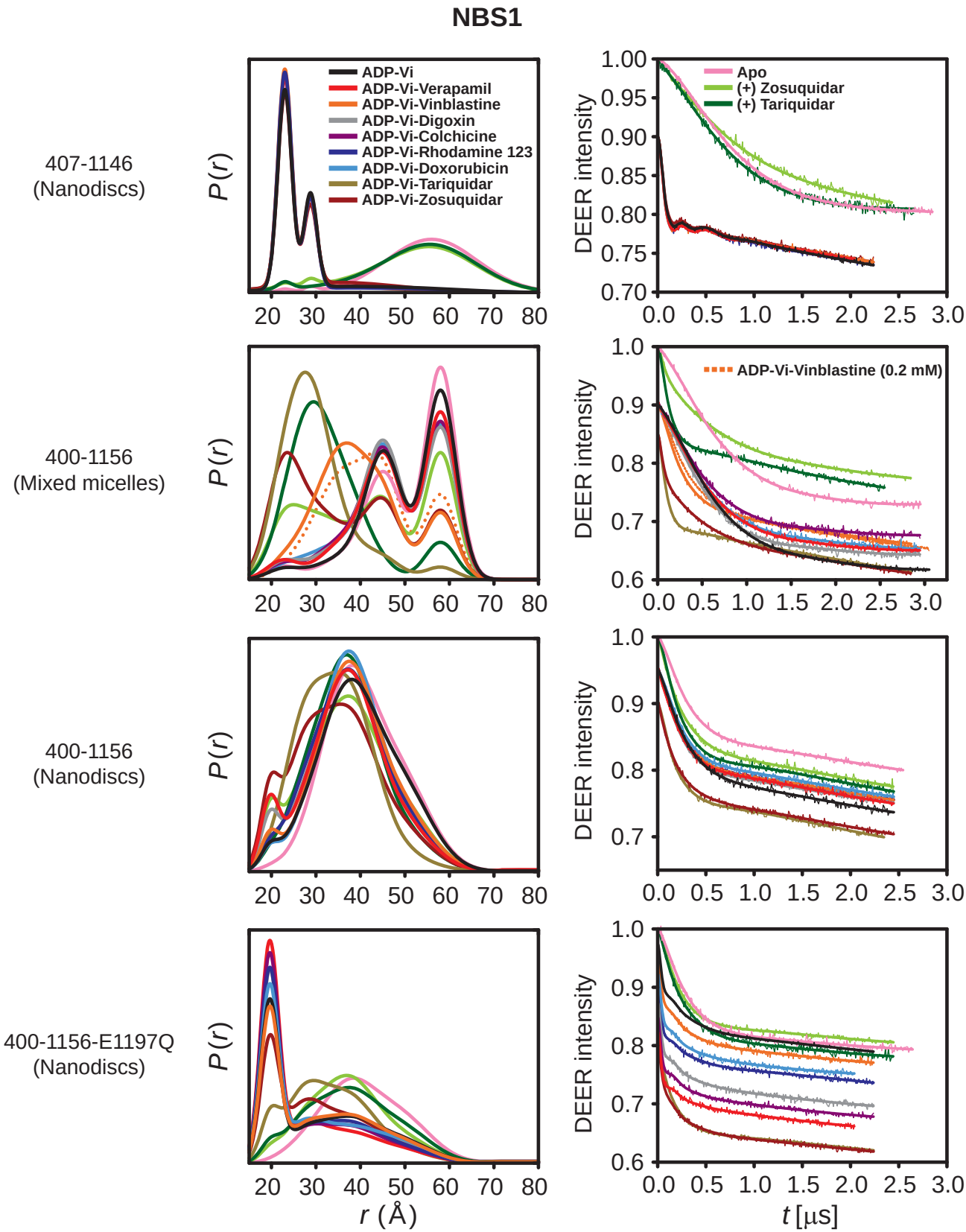

Data Appendix 3. DEER data analysis for the nucleotide binding site 1 (NBS1). For each mutant, from left to right, distance distributions, and the primary DEER traces along with the fits are shown. Normalized DEER traces are shown with y-axis offsets for clarity. In addition, 500 ns at the end of DEER traces are removed (not shown) to reduce the contribution of the artefacts at the end of the trace which could disturb data analysis.

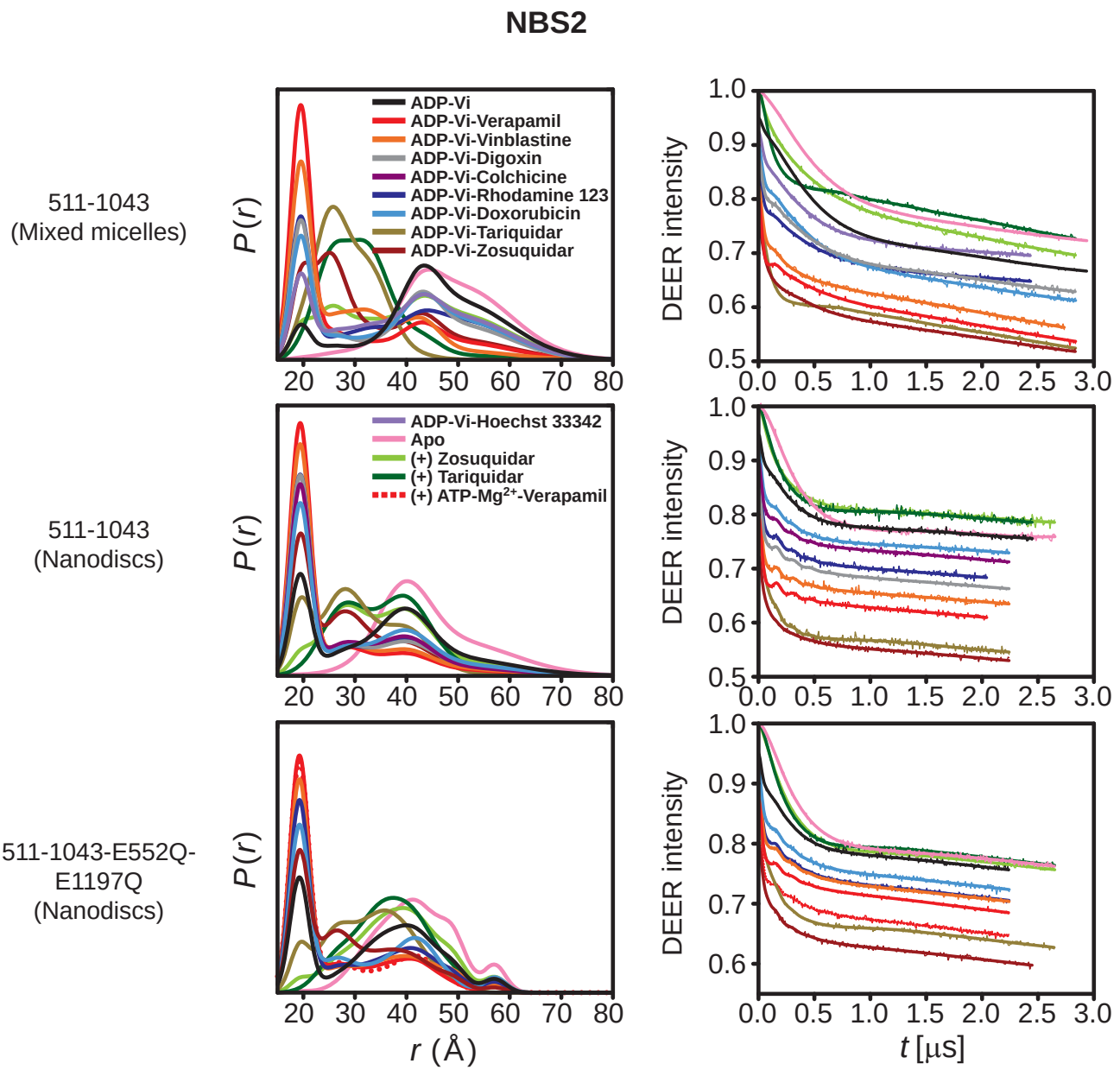

Data Appendix 4. DEER data analysis for the nucleotide binding site 2 (NBS2). For each mutant, from left to right, distance distributions, and the primary DEER traces along with the fits are shown. Normalized DEER traces are shown with y-axis offsets for clarity. In addition, 500 ns at the end of DEER traces are removed (not shown) to reduce the contribution of the artefacts at the end of the trace which could disturb data analysis.

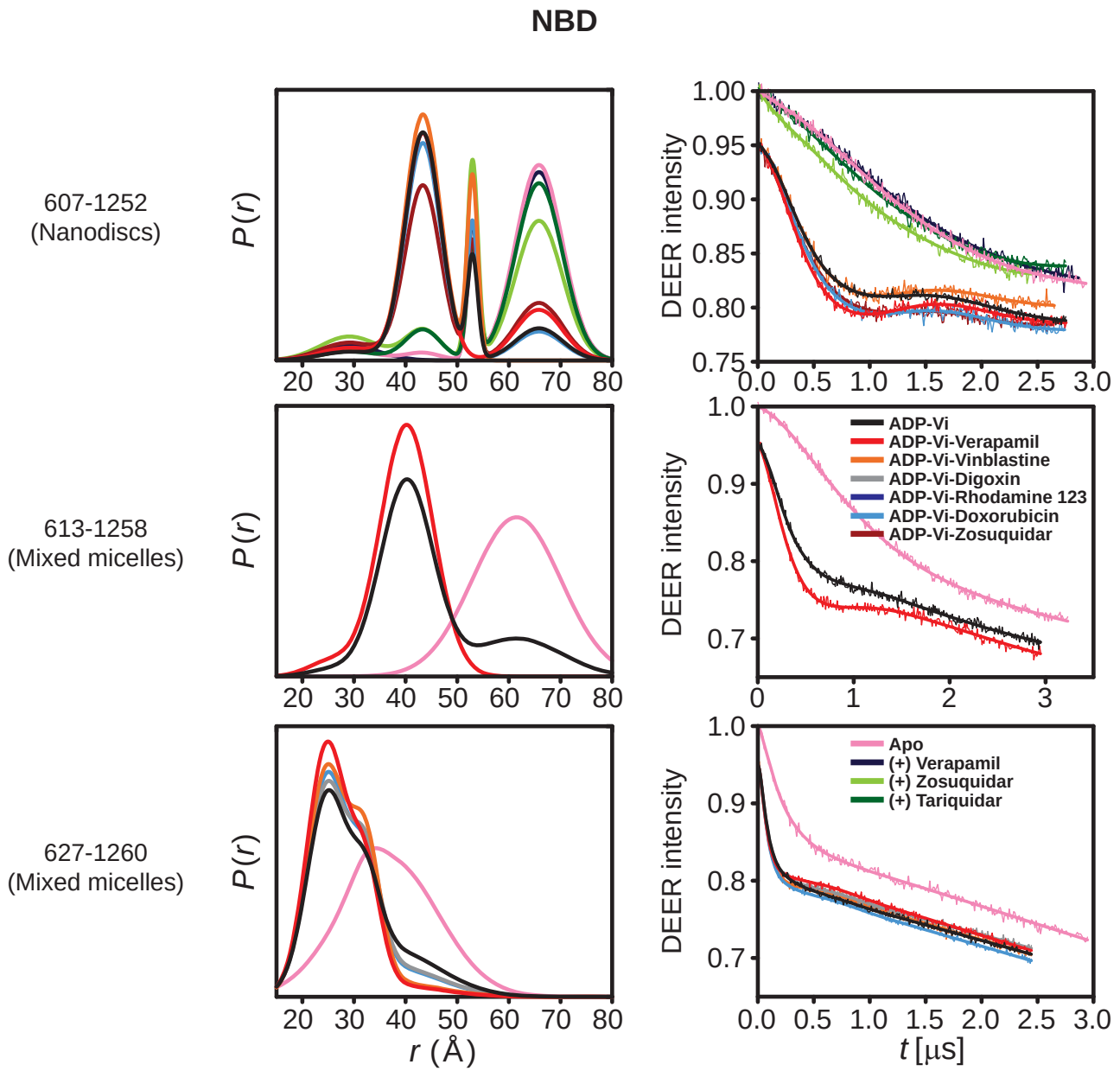

Data Appendix 5. DEER data analysis for the nucleotide binding domain (NBD). For each mutant, from left to right, distance distributions, and the primary DEER traces along with the fits are shown. Normalized DEER traces are shown with y-axis offsets for clarity. In addition, 500 ns at the end of DEER traces are removed (not shown) to reduce the contribution of the artefacts at the end of the trace which could disturb data analysis.

References and Notes

1. F. J. Sharom, ABC multidrug transporters: Structure, function and role in chemoresistance. *Pharmacogenomics* **9**, 105–127 (2008). doi:10.2217/14622416.9.1.105 Medline

2. R. J. Ferreira, C. A. Bonito, M. J. U. Ferreira, D. J. V. A. dos Santos, About P-glycoprotein: A new drugable domain is emerging from structural data. *Wiley Interdiscip. Rev. Comput. Mol. Sci.* **7**, e1316 (2017). doi:10.1002/wcms.1316

3. D. C. Rees, E. Johnson, O. Lewinson, ABC transporters: The power to change. *Nat. Rev. Mol. Cell Biol.* **10**, 218–227 (2009). doi:10.1038/nrm2646 Medline

4. K. P. Locher, Mechanistic diversity in ATP-binding cassette (ABC) transporters. *Nat. Struct. Mol. Biol.* **23**, 487–493 (2016). doi:10.1038/nsmb.3216 Medline

5. D. Szöllősi, D. Rose-Sperling, U. A. Hellmich, T. Stockner, Comparison of mechanistic transport cycle models of ABC exporters. *Biochim. Biophys. Acta Biomembr.* **1860**, 818–832 (2018). doi:10.1016/j.bbamem.2017.10.028 Medline

6. N. M. I. Taylor, I. Manolaridis, S. M. Jackson, J. Kowal, H. Stahlberg, K. P. Locher, Structure of the human multidrug transporter ABCG2. *Nature* **546**, 504–509 (2017). doi:10.1038/nature22345 Medline

7. Z. L. Johnson, J. Chen, Structural Basis of Substrate Recognition by the Multidrug Resistance Protein MRP1. *Cell* **168**, 1075–1085.e9 (2017). doi:10.1016/j.cell.2017.01.041 Medline

8. B. Verhalen, R. Dastvan, S. Thangapandian, Y. Peskova, H. A. Koteiche, R. K. Nakamoto, E. Tajkhorshid, H. S. Mchaourab, Energy transduction and alternating access of the mammalian ABC transporter P-glycoprotein. *Nature* **543**, 738–741 (2017). doi:10.1038/nature21414 Medline

9. K. Barth, S. Hank, P. E. Spindler, T. F. Prisner, R. Tampé, B. Joseph, Conformational Coupling and trans-Inhibition in the Human Antigen Transporter Ortholog TmrAB Resolved with Dipolar EPR Spectroscopy. *J. Am. Chem. Soc.* **140**, 4527–4533 (2018). doi:10.1021/jacs.7b12409 Medline

10. M. E. Zoghbi, L. Mok, D. J. Swartz, A. Singh, G. A. Fendley, I. L. Urbatsch, G. A. Altenberg, Substrate-induced conformational changes in the nucleotide-binding domains of lipid bilayer-associated P-glycoprotein during ATP hydrolysis. *J. Biol. Chem.* **292**, 20412–20424 (2017). doi:10.1074/jbc.M117.814186 Medline

11. S. Mishra, B. Verhalen, R. A. Stein, P.-C. Wen, E. Tajkhorshid, H. S. Mchaourab, Conformational dynamics of the nucleotide binding domains and the power stroke of a heterodimeric ABC transporter. *eLife* **3**, e02740 (2014). doi:10.7554/eLife.02740

12. A. Alam, R. Küng, J. Kowal, R. A. McLeod, N. Tremp, E. V. Broude, I. B. Roninson, H. Stahlberg, K. P. Locher, Structure of a zosuquidar and UIC2-bound human-mouse chimeric ABCB1. *Proc. Natl. Acad. Sci. U.S.A.* **115**, E1973–E1982 (2018). doi:10.1073/pnas.1717044115 Medline

13. L. Esser, F. Zhou, K. M. Pluchino, J. Shiloach, J. Ma, W. K. Tang, C. Gutierrez, A. Zhang, S. Shukla, J. P. Madigan, T. Zhou, P. D. Kwong, S. V. Ambudkar, M. M. Gottesman, D.

Xia, Structures of the Multidrug Transporter P-glycoprotein Reveal Asymmetric ATP Binding and the Mechanism of Polyspecificity. *J. Biol. Chem.* **292**, 446–461 (2017). doi:10.1074/jbc.M116.755884 Medline

14. J. Li, K. F. Jaimes, S. G. Aller, Refined structures of mouse P-glycoprotein. *Protein Sci.* **23**, 34–46 (2014). doi:10.1002/pro.2387 Medline

15. M. K. Al-Shawi, M. K. Polar, H. Omote, R. A. Figler, Transition state analysis of the coupling of drug transport to ATP hydrolysis by P-glycoprotein. *J. Biol. Chem.* **278**, 52629–52640 (2003). doi:10.1074/jbc.M308175200 Medline

16. G. Tombline, A. E. Senior, The occluded nucleotide conformation of p-glycoprotein. *J. Bioenerg. Biomembr.* **37**, 497–500 (2005). doi:10.1007/s10863-005-9498-4 Medline

17. G. Tombline, J. J. Holt, M. K. Gannon, D. J. Donnelly, B. Wetzel, G. A. Sawada, T. J. Raub, M. R. Detty, ATP occlusion by P-glycoprotein as a surrogate measure for drug coupling. *Biochemistry* **47**, 3294–3307 (2008). doi:10.1021/bi7021393 Medline

18. A. Siarheyeva, R. Liu, F. J. Sharom, Characterization of an asymmetric occluded state of P-glycoprotein with two bound nucleotides: Implications for catalysis. *J. Biol. Chem.* **285**, 7575–7586 (2010). doi:10.1074/jbc.M109.047290 Medline

19. E. Janas, M. Hofacker, M. Chen, S. Gompf, C. van der Does, R. Tampé, The ATP hydrolysis cycle of the nucleotide-binding domain of the mitochondrial ATP-binding cassette transporter Mdl1p. *J. Biol. Chem.* **278**, 26862–26869 (2003). doi:10.1074/jbc.M301227200 Medline

20. G. Jeschke, DEER distance measurements on proteins. *Annu. Rev. Phys. Chem.* **63**, 419–446 (2012). doi:10.1146/annurev-physchem-032511-143716 Medline

21. H. S. Mchaourab, P. R. Steed, K. Kazmier, Toward the fourth dimension of membrane protein structure: Insight into dynamics from spin-labeling EPR spectroscopy. *Structure* **19**, 1549–1561 (2011). doi:10.1016/j.str.2011.10.009 Medline

22. O. Schiemann, T. F. Prisner, Long-range distance determinations in biomacromolecules by EPR spectroscopy. *Q. Rev. Biophys.* **40**, 1–53 (2007). doi:10.1017/S003358350700460X Medline

23. I. L. Urbatsch, B. Sankaran, S. Bhagat, A. E. Senior, Both P-glycoprotein nucleotide-binding sites are catalytically active. *J. Biol. Chem.* **270**, 26956–26961 (1995). doi:10.1074/jbc.270.45.26956 Medline

24. M. L. Oldham, J. Chen, Snapshots of the maltose transporter during ATP hydrolysis. *Proc. Natl. Acad. Sci. U.S.A.* **108**, 15152–15156 (2011). doi:10.1073/pnas.1108858108 Medline

25. Y. Kim, J. Chen, Molecular structure of human P-glycoprotein in the ATP-bound, outward-facing conformation. *Science* **359**, 915–919 (2018). doi:10.1126/science.aar7389 Medline

26. S. Shukla, B. Abel, E. E. Chufan, S. V. Ambudkar, Effects of a detergent micelle environment on P-glycoprotein (ABCB1)-ligand interactions. *J. Biol. Chem.* **292**, 7066–7076 (2017). doi:10.1074/jbc.M116.771634 Medline

27. S. V. Ambudkar, I. W. Kim, D. Xia, Z. E. Sauna, The A-loop, a novel conserved aromatic acid subdomain upstream of the Walker A motif in ABC transporters, is critical for ATP binding. *FEBS Lett.* **580**, 1049–1055 (2006). doi:10.1016/j.febslet.2005.12.051 Medline

28. W. D. Stein, C. Cardarelli, I. Pastan, M. M. Gottesman, Kinetic evidence suggesting that the multidrug transporter differentially handles influx and efflux of its substrates. *Mol. Pharmacol.* **45**, 763–772 (1994). Medline

29. E. E. Chufan, K. Kapoor, S. V. Ambudkar, Drug-protein hydrogen bonds govern the inhibition of the ATP hydrolysis of the multidrug transporter P-glycoprotein. *Biochem. Pharmacol.* **101**, 40–53 (2016). doi:10.1016/j.bcp.2015.12.007 Medline

30. T. W. Loo, D. M. Clarke, Tariquidar inhibits P-glycoprotein drug efflux but activates ATPase activity by blocking transition to an open conformation. *Biochem. Pharmacol.* **92**, 558–566 (2014). doi:10.1016/j.bcp.2014.10.006 Medline

31. P. Zou, H. S. McHaourab, Increased sensitivity and extended range of distance measurements in spin-labeled membrane proteins: Q-band double electron-electron resonance and nanoscale bilayers. *Biophys. J.* **98**, L18–L20 (2010). doi:10.1016/j.bpj.2009.12.4193 Medline

32. Smriti, P. Zou, H. S. McHaourab, Mapping daunorubicin-binding Sites in the ATP-binding cassette transporter MsbA using site-specific quenching by spin labels. *J. Biol. Chem.* **284**, 13904–13913 (2009). doi:10.1074/jbc.M900837200 Medline

33. G. Jeschke, Y. Polyhach, Distance measurements on spin-labelled biomacromolecules by pulsed electron paramagnetic resonance. *Phys. Chem. Chem. Phys.* **9**, 1895–1910 (2007). doi:10.1039/b614920k Medline

34. R. A. Stein, A. H. Beth, E. J. Hustedt, A Straightforward Approach to the Analysis of Double Electron-Electron Resonance Data. *Methods Enzymol.* **563**, 531–567 (2015). doi:10.1016/bs.mie.2015.07.031 Medline

35. E. J. Hustedt, F. Marinelli, R. A. Stein, J. D. Faraldo-Gómez, H. S. Mchaourab, Confidence Analysis of DEER Data and Its Structural Interpretation with Ensemble-Biased Metadynamics. *Biophys. J.* **115**, 1200–1216 (2018). doi:10.1016/j.bpj.2018.08.008 Medline

36. Y. Polyhach, E. Bordignon, G. Jeschke, Rotamer libraries of spin labelled cysteines for protein studies. *Phys. Chem. Chem. Phys.* **13**, 2356–2366 (2011). doi:10.1039/C0CP01865A Medline